Reconstruction of the Acoustic Field Radiated Directly from a Vibrating Structure Located Near a Pressure-Release Boundary

Zhimin Chen

College of Naval Architecture and Ocean Engineering, Naval University of Engineering, 717 Jiefang Road, Wuhan 430033, China.

Daren Zhou

Sound and Vibration Laboratory, College of Mechanical Engineering, Zhejiang University of Technology, 18 Chaowang Road, Hangzhou 310014, China. E-mail: zhoudaren_svlab@163.com

Jingjun Lou

College of Naval Architecture and Ocean Engineering, Naval University of Engineering, 717 Jiefang Road, Wuhan 430033, China.

Near-field acoustical holography is a powerful tool for reconstructing the three-dimensional acoustic field radiated from a vibrating structure located in free space, but it is not applicable when the source is in a half space bounded by a reflecting boundary. This paper develops a method based on half-space spherical wave function expansion for reconstructing the acoustic field radiated directly from a source located near a pressure-release boundary. First, the series of half-space spherical wave basis functions satisfying the pressure-release boundary condition is formulated. Then the acoustic field in a half space is modeled using an expansion in this basis. The expansion coefficients are determined by solving an overdetermined linear system of equations, obtained by matching this expansion to the measured half-space acoustic pressures. The pressures radiated directly from the source can finally be reconstructed using the free-space spherical wave function expansion with the obtained expansion coefficients. Numerical simulation examples of a vibrating plate located in water near a pressure-release boundary are demonstrated to validate the proposed method. The effects of various parameters, such as the acoustic frequency, the distance between the source and boundary, and the orientation of the source surface, on the reconstruction accuracy are examined.

1. INTRODUCTION

The level of acoustic pressure radiated from underwater vehicles, such as submarines, is an important criterion for evaluating their performance. To three-dimensionally visualize the acoustic quantities generated by a vehicle using near-field acoustical holography (NAH),[1] the first step is to accurately measure the acoustic quantities with an array of sensors. The ideal environment for the measurements is free space, which is not always available. In many cases, the measurements must be implemented in an enclosed space or a semi-closed space bounded by reflecting surfaces. Consequently, the measured quantities include contributions from both the direct radiation from the source and the boundary reflection. These data do not immediately provide correct information about the source radiation. Nor can they be used directly as inputs to the NAH algorithms,[2–4] because all the methods for NAH implementation are proposed based on the assumption that the sensor array is placed in a source-free region.[1]

To realize the visualization of direct radiation from a source in the presence of a reflecting boundary, methods for half-space acoustic field reconstruction based on different NAH implementations are proposed. By replacing the free-space Green's function with a half-space Green's function in the formulation of the equivalent source method (ESM), the reconstruction of the acoustic quantities on the source surface in a half space bounded by an impedance plane is realized.[5–7] Using a similar replacement of the Green's function, the acoustic quantities generated by a structure located near a rigid plane are reconstructed using the inverse boundary element method.[8] The acoustic field radiated directly from a planar source facing a parallel impedance plane is reconstructed using Fourier acoustics,[9] and the half-space acoustic pressure is modeled as the superposition of a series of plane waves and the reflection due to each plane-wave component. In addition to the above reconstruction of the stationary acoustic field, the reconstruction of the transient field above an impedance plane is also studied.[10] A transient half-space Green's function is utilized in the ESM to model the acoustic field above the plane.

Recently, a series of half-space spherical wave basis functions is formulated and utilized to replace the free-space spherical wave basis functions in the Helmholtz equation least-squares (HELS) method.[11–13] The direct radiation from a source located near an impedance boundary is then reconstructed. In this paper, we consider the problem of reconstructing the direct radiation from a vibrating structure located near a pressure-release boundary.[5,14] The method proposed here is
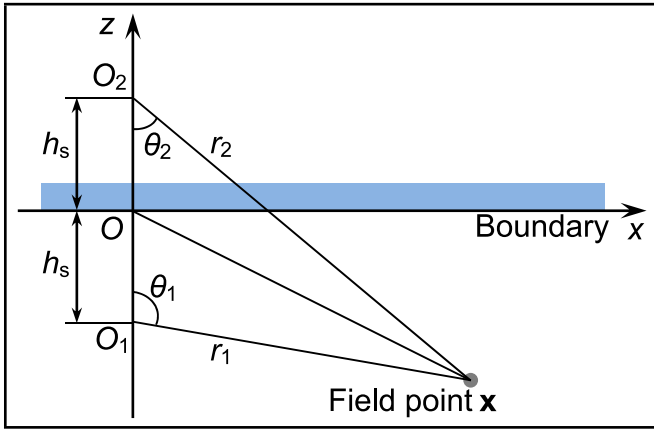
Figure 1. Geometry of a multipole source and a field point.

also based on the expansion in half-space spherical wave functions.

The pressure-release boundary, also known as the Dirichlet boundary, is commonly encountered in underwater acoustics.[5] For example, in a semi-enclosed space for measurement of acoustic radiation from underwater vehicles, the upper water-air interface can be viewed as a natural pressure-release boundary.[14] If the vibrating surface of the vehicle is close to this interface, the measured quantities will inevitably be polluted by the interface reflection. Hence, it is necessary to develop a method applicable to the half-space problem with a pressure-release boundary, though little literature focuses on this problem so far. Moreover, the acoustic field near a pressure-release boundary shows totally different physical behaviors from that near an impedance boundary or a rigid boundary. Consequently, different half-space spherical wave functions need to be formulated.

2. MATHEMATICAL MODELING

2.1. Formulation of Half-Space Spherical Wave Functions

HELS-based NAH employs the superposition of free-space spherical wave basis functions to model the acoustic field generated by a vibrating structure located in free space.[11] Accordingly, to implement an acoustic field reconstruction in a half space with a pressure-release boundary, the half-space spherical wave basis functions needed to be formulated.[12] We first considered the solution to the acoustic field generated by a monopole source located in this half space.

As shown in Fig. 1, the monopole source and its mirror image about the boundary were at O_1 and O_2, respectively. A global coordinate system with the origin O placed on the boundary was established, such that the global coordinates of O_1 and O_2 were given by $\mathbf{x}_{O_1} = (0,\ 0,\ -h_s)$ and $\mathbf{x}_{O_2} = (0,\ 0, h_s)$, respectively. The half-space acoustic pressure $p_{\text{half}}^{(0)}(\mathbf{x};\omega)$ at a field point $\mathbf{x}$ satisfied the inhomogeneous Helmholtz equation:[12]

$$\nabla^2 p_{\text{half}}^{(0)}(\mathbf{x};\omega) + k^2 p_{\text{half}}^{(0)}(\mathbf{x};\omega) = -S_0 \delta(\mathbf{x} - \mathbf{x}_{O_1});\quad (1)$$

where ∇^2 was the Laplace operator; k was the acoustic wavenumber; $\omega = 2\pi f$ was the angular frequency in rad/s; f was the frequency in Hz; a time-harmonic function of the form $e^{-i\omega t}$ was assumed with $i = \sqrt{-1}$; $\delta(\mathbf{x} - \mathbf{x}_{O_1})$ was the Dirac delta function. On the boundary $z = 0$, the acoustic pressure $p_{\text{half}}^{(0)}(\mathbf{x};\omega)$ satisfies the pressure-release boundary condition,[14]

$$p_{\text{half}}^{(0)}(x, y, 0;\omega) = 0. \quad (2)$$

The governing equation (1) along with the boundary condition Eq. (2) can be solved using the method of images,[5] as

$$p_{\text{half}}^{(0)}(\mathbf{x};\omega) = \frac{S_0}{4\pi}\left(\frac{e^{ikr_1}}{r_1} - \frac{e^{ikr_2}}{r_2}\right); \quad (3)$$

where r_1 and r_2 were the distances from the field point $\mathbf{x}$ to the monopole location $\mathbf{x}_{O_1}$ and its mirror image $\mathbf{x}_{O_2}$. The minus sign between the two terms was used to satisfy the pressure-release boundary condition.

From Eq. (3), it was found that the incident spherical wave due to a monopole was reflected by the pressure-release boundary with a constant reflection coefficient -1. Since each term of the free-space spherical wave functions represented the acoustic radiation from a multipole or a set of multipoles,[1,5,12] which was constructed from distributions of monopoles, one can formulate the half-space spherical wave functions as

$$\psi_{\text{j half}}(\mathbf{x};\omega) = \psi_j(\mathbf{x},\mathbf{x}_{O_1};\omega) + (-1)\cdot\psi_j(\mathbf{x}, \mathbf{x}_{O_2};\omega);\quad (4)$$

where $\psi_j(\mathbf{x},\mathbf{x}_{O_1};\omega)$ and $\psi_j(\mathbf{x}, \mathbf{x}_{O_2};\omega)$ were the jth term of the free-space spherical wave functions,[11,12] representing the acoustic radiation from a multipole or a set of multipoles located at $\mathbf{x}_{O_1}$, and the corresponding image sources located at $\mathbf{x}_{O_2}$, respectively. The free-space spherical wave functions ψ_j were solutions to the Helmholtz equation, expressible in spherical coordinates as[11]

$$\psi_j(\mathbf{x};\omega) \equiv \psi_{nl}(r, \theta, \phi;\omega) = h_n^{(1)}(kr) Y_n^l(\theta, \phi);\quad (5)$$

where $h_n^{(1)}(kr)$ were the spherical Hankel functions of the first kind, and $Y_n^l(\theta, \phi)$ were the spherical harmonics. The indices n, l and j in Eq. (5) were related by $j = n^2 + n + l + 1$, with n ranging from 0 to N and l from $-n$ to n. As shown in Fig. 1, two local coordinate systems, with the origins O_1 and O_2, are established by translations of the global coordinate system. For a field point in the half space, the local coordinates $\mathbf{x}_1 \equiv (r_1, \theta_1, \phi_1)$ with origin O_1 and $\mathbf{x}_2 \equiv (r_2, \theta_2, \phi_2)$ with origin O_2 were related to global coordinates $\mathbf{x}$ through the following relationships:

$$\mathbf{x}_1 = \mathbf{x} + h_s\mathbf{e}_z,\ \mathbf{x}_2 = \mathbf{x} - h_s\mathbf{e}_z;\quad (6)$$

where $\mathbf{e}_z$ was the unit vector in the z direction. The half-space spherical wave functions (Eq. (4)) satisfy the Helmholtz equation, along with the pressure-release boundary condition. On the right side of Eq. (4), for a constant index j, the first and second terms represented a component contributing to the direct radiation from the source and the boundary reflection, respectively.

2.2. Expansion in Half-Space Spherical Wave Functions

As shown in Fig. 2, when the vibrating structure is located near an infinite plane with a pressure-release boundary, the half-space acoustic pressure $p_{\text{half}}(\mathbf{x};\omega)$ at a field point $\mathbf{x}$ can
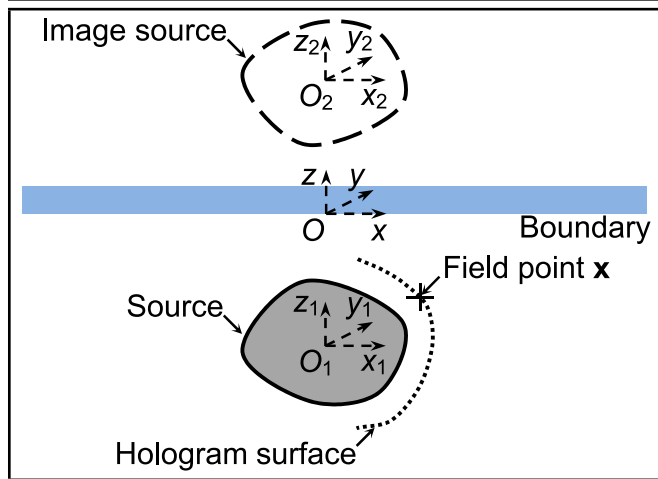
Figure 2. Schematic of the half-space acoustic field generated by a vibrating structure located near a pressure-release boundary.

be expressed using the superposition of half-space spherical wave functions as

$$p_{\text{half}}(\mathbf{x};\omega) \approx \sum_{j=1}^{J} c_j(\omega)\,\psi_{j\,\text{half}}(\mathbf{x};\omega); \qquad (7)$$

where $\psi_{j\,\text{half}}(\mathbf{x};\omega)$ were the half-space spherical wave functions (see Eq. (4)); $c_j(\omega)$ were the coefficients of the expansion; j was the index of the expansion term, ranging from 1 to J; and J was the number of terms retained in the expansion.

If an array of M measurement points was utilized as the hologram surface, then we have

$$\{p_{\text{half}}^{\text{meas}}(\mathbf{x}_m;\omega)\}_{M\times 1} = [\psi_{\text{half}}(\mathbf{x}_m;\omega)]_{M\times J}\,\{c(\omega)\}_{J\times 1}; \quad (8)$$

where $\{p_{\text{half}}^{\text{meas}}(\mathbf{x}_m;\omega)\}_{M\times 1}$ was a column vector of the measured half-space acoustic pressures; the vectors $\mathbf{x}_m$, $m = 1$ to M, denoted the locations of measurement points; $[\psi_{\text{half}}(\mathbf{x}_m;\omega)]_{M\times J}$ was a matrix of the half-space spherical wave functions, calculated at $\mathbf{x}_m$; and $\{c(\omega)\}_{J\times 1}$ was a column vector of the coefficients of the expansion functions. The number of measurement points was in general larger than the number of expansion terms, so the expansion coefficients can be determined by taking the pseudo-inverse of the expansion matrix,

$$\{c(\omega)\}_{J\times 1} = [\psi_{\text{half}}(\mathbf{x}_m;\omega)]_{J\times M}^{\dagger}\,\{p_{\text{half}}^{\text{meas}}(\mathbf{x}_m;\omega)\}_{M\times 1}; \quad (9)$$

where the superscript † denoted the pseudo-inverse of a matrix, given by

$$[\psi_{\text{half}}(\mathbf{x}_m;\omega)]_{J\times M}^{\dagger} =$$
$$\left([\psi_{\text{half}}(\mathbf{x}_m;\omega)]_{J\times M}^{H}\,[\psi_{\text{half}}(\mathbf{x}_m;\omega)]_{M\times J}\right)^{-1}$$
$$\times\,[\psi_{\text{half}}(\mathbf{x}_m;\omega)]_{J\times M}^{H}; \qquad (10)$$

where the superscript H denoted the conjugate transpose of a matrix. Once the coefficients $\{c(\omega)\}_{J\times 1}$ in Eq. (8) were determined, the half-space acoustic pressures and the acoustic pressures radiated directly from the source at any points $\mathbf{x}_s$, including those on the source surface, can be reconstructed, respectively, by

$$\{p_{\text{half}}^{\text{rec}}(\mathbf{x}_s;\omega)\}_{S\times 1} = [\psi_{\text{half}}(\mathbf{x}_s;\omega)]_{S\times J}\,\{c(\omega)\}_{J\times 1}; \quad (11)$$

$$\{p^{\text{rec}}(\mathbf{x}_s;\omega)\}_{S\times 1} = [\psi(\mathbf{x}_s,\mathbf{x}_{O_1};\omega)]_{S\times J}\,\{c(\omega)\}_{J\times 1}; \quad (12)$$

where $\{p_{\text{half}}^{\text{rec}}(\mathbf{x}_s;\omega)\}_{S\times 1}$ was a column vector of the reconstructed half-space acoustic pressures; the vectors $\mathbf{x}_s$, $s = 1$ to S, denote the locations of reconstruction points; $[\psi_{\text{half}}(\mathbf{x}_s;\omega)]_{S\times J}$ was a matrix of the half-space spherical wave functions, calculated at $\mathbf{x}_s$; $\{p^{\text{rec}}(\mathbf{x}_s;\omega)\}_{S\times 1}$ was a column vector of the reconstructed acoustic pressures, radiated directly from the source; and $[\psi(\mathbf{x}_s,\mathbf{x}_{O_1};\omega)]_{S\times J}$ was a matrix of the free-space spherical wave functions, calculated at $\mathbf{x}_s$. Equation (12) was the main result of this paper.

The procedures for the determination of the number of expansion terms were as follows. The half-space acoustic pressures at a subset of measurement points were used to determine the expansion coefficients. Then the acoustic pressures at the other subset of measurement points were reconstructed using Eq. (11). The reconstruction was repeated for different values of J. The minimum least-squares error between the reconstructed pressures and the measured pressures was utilized as a criterion to obtain the optimal value J_{opt}. Mathematically, this process was expressed as

$$\frac{\left\|\{p_{\text{half}}^{\text{rec}}(\mathbf{x}_{m'};\omega)\}_{\lfloor\frac{M}{2}\rfloor\times 1} - \{p_{\text{half}}^{\text{meas}}(\mathbf{x}_{m'};\omega)\}_{\lfloor\frac{M}{2}\rfloor\times 1}\right\|_2}{\left\|\{p_{\text{half}}^{\text{meas}}(\mathbf{x}_{m'};\omega)\}_{\lfloor\frac{M}{2}\rfloor\times 1}\right\|_2}; \quad (13)$$

where $\|\cdot\|_2$ denoted the 2-norm; the vectors $\mathbf{x}_{m'}$, $m' = 1, 2, \ldots, \lfloor\frac{M}{2}\rfloor$, denoted the locations of the subset of measurement points, at which the acoustic pressures are reconstructed; and $\lfloor\cdot\rfloor$ denotes that the fraction is rounded down.

In addition, a modified Tikhonov regularization, implemented through singular value decomposition (SVD), was used in this study.[2,8] The regularization parameter is determined by the generalized cross-validation (GCV).[2,8]

3. NUMERICAL SIMULATIONS

Numerical simulation examples were demonstrated to validate the proposed method and examine the effects of various parameters on the reconstruction accuracy. A baffled plate was chosen as the source structure. In the simulations, a surface velocity distribution of the vibrating plate was prescribed. The acoustic pressures radiated from the source located in free space were used as benchmark values, which were calculated using Rayleigh's integral.[1] The acoustic pressures (simulated measurements) found on the hologram surface in the half space were used as input data to the proposed reconstruction algorithm. This half-space acoustic pressure was also calculated by using Rayleigh's integral, once the surface velocity distribution of the vibrating plate is given. The premise was that the free-space Green's function in Rayleigh's integral was replaced by the half-space Green's function satisfying the pressure-release boundary condition.[1,5,15] The reconstructed acoustic pressures radiated directly from the source, obtained from Eq. (12), were compared with the benchmark values to validate the proposed method. The assumed fluid density and speed of sound were $\rho_0 = 1000$ kg/m^3 and $c = 1500$ m/s, respectively.

To quantify the reconstruction accuracy, normalized relative reconstruction percentage error on the reconstruction surface
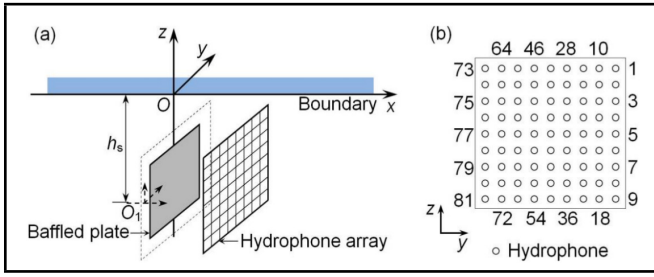
Figure 3. Schematic of acoustic pressure measurements for a baffled plate located near a pressure-release boundary: (a) the geometry of the source and hydrophone array; (b) the indices of the hydrophones mounted on the array.

was defined as

$$\varepsilon = \frac{\left\| \{p^{\mathrm{rec}}(\mathbf{x}_s;\omega)\}_{S\times 1} - \{p^{\mathrm{ben}}(\mathbf{x}_s;\omega)\}_{S\times 1} \right\|_2}{\left\| \{p^{\mathrm{ben}}(\mathbf{x}_s;\omega)\}_{S\times 1} \right\|_2} \times 100\%; \tag{14}$$

where $\{p^{\mathrm{ben}}(\mathbf{x}_s;\omega)\}_{S\times 1}$ is a column vector of the benchmark acoustic pressures. The sound power ratio of the direct radiation relative to the boundary reflection at the measurement points is defined as[12]

$$\eta = 20\,\frac{\left\| \{p^{\mathrm{ben}}(\mathbf{x}_m;\omega)\}_{M\times 1} \right\|_2}{\left\| \{p^{\mathrm{refl}}(\mathbf{x}_m;\omega)\}_{M\times 1} \right\|_2}\,(\mathrm{dB})\,; \tag{15}$$

where $\{p^{\mathrm{refl}}(\mathbf{x}_m;\omega)\}_{M\times 1}$ was a column vector of the boundary-reflected acoustic pressures. The ratio η was defined to measure the relative proportion of the direct radiation and boundary reflection in the half-space acoustic pressures measured by the array. It was a critical parameter and will be discussed in the analyses of reconstruction accuracy.

3.1. Validation of the Proposed Method

Figure 3(a) illustrates the setup of the baffled plate, the hydrophone array, and the pressure-release boundary. Various parameters involved in the numerical simulations were chosen as follows. The square plate, with a length of one side $L = 0.4$ m, was located on the y-z plane. The distance from the geometrical center of the plate surface to the pressure-release boundary was $h_s = 0.4$ m. The plate was dilating like a piston, with an amplitude of surface velocity $V_0 = 1.0 \times 10^{-3}$ m/s. Following the guidelines for implementing the HELS-based NAH method,[16] the origin O_1 was set by moving the geometrical center of the plate surface a distance $d_0 = 0.9\sqrt{\left(\frac{L}{2}\right)^2 + \left(\frac{L}{2}\right)^2}$ in the negative x direction.

The half-space acoustic pressures were measured in simulation by a planar hydrophone array parallel to the plate surface, at a standoff distance $d_s = 0.05$ m from the surface. The distance from the geometrical center of the array to the boundary was also h_s. The aperture of the array is 0.52 m $\times$ 0.52 m, on which 81 measurement points were regularly distributed with spacing of 0.065 m. As shown in Fig. 3(b), to assist our discussion of the results, an index was assigned to each of the 81 measurement points, where the point located at (0.05 m, 0.26 m, -0.14 m) was marked as Sensor 1, and the point located at (0.05 m, -0.26 m, -0.66 m) was Sensor 81. White noise with a signal-to-noise ratio of 30 dB is added to the measured acoustic pressures.
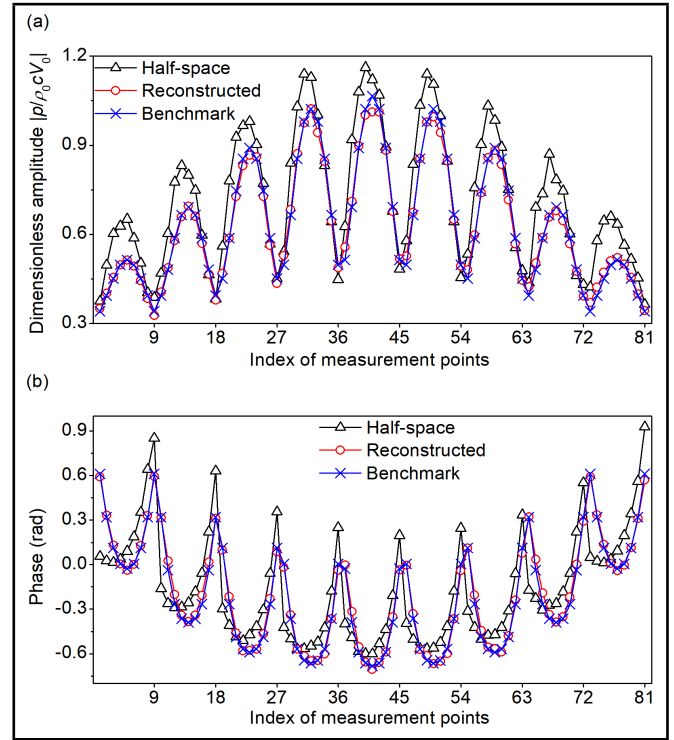
Figure 4. Comparison of the half-space acoustic pressure distribution, the reconstructed acoustic pressure distribution using the proposed method, and the benchmark distribution, for $f = 1500$ Hz: (a) amplitude; (b) phase.

Figure 4 shows the acoustic pressure distributions at the measurement points, including the half-space acoustic pressure distribution, the reconstructed value distribution obtained using the proposed method, and the benchmark distribution radiated directly from the plate, for a frequency $f = 1500$ Hz. From the amplitude distributions shown in Fig. 4(a), it was found that the half-space acoustic pressure distribution was much different from the benchmark distribution. The half-space amplitudes were even smaller than the benchmark amplitudes at some points. As shown in Fig. 4(b), the phase distribution of half-space acoustic pressures also differs from that of the benchmark values. The differences indicated that the boundary reflection has a great influence on the measured acoustic pressures on the hologram surface. Thus, the measured values cannot reflect the real acoustic radiation from the source.

After using the proposed method, the reconstructed amplitude and phase distributions agreed well with the corresponding benchmark distributions, as shown in Figs. 4(a) and 4(b). In this simulation example, the reconstruction error ε was 3.81%. The results demonstrate that the proposed method successfully eliminates the effect of the pressure-release boundary reflection, and reconstructs the acoustic pressures radiated directly from the plate with high accuracy.

3.2. Effect of the Vertical Distance Between the Source and Boundary

The accuracy in reconstruction when the plate was vibrating at different frequencies and located at different vertical distances from the boundary is investigated. The frequencies of interest were $f = 100$ Hz $\sim$ 2100 Hz. Three different vertical distances, $h_s = L$, $1.2L$, and $1.4L$, were considered. At these distances, the curves of reconstruction error versus frequency

show different trends, so that the influence of vertical distance on reconstruction accuracy can be revealed. Note that the geometrical centers of the array and the plate surface were always kept at the same vertical height h_s in the simulation examples. Other parameters remained unchanged, as presented in Section 3.1.

The reconstruction errors ε versus frequency f, calculated at different vertical distances h_s, are shown in Fig. 5(a). When the vertical distance $h_s = L$, the reconstruction error ε first declined and then grew with the increase of frequency f. When h_s increased to $1.2L$, ε also showed a decline first, and then grows. However, the rate of decline was smaller than that obtained when $h_s = L$. When $h_s = 1.4L$, the reconstruction error ε no longer obviously declined in the low-frequency range. Instead, the curve of ε first showed a small rate of variation and then grew monotonically with the increase of frequency f. In addition, for most frequencies, the reconstruction errors ε were reduced with the increase of vertical distance h_s.

Two dominant factors affecting the reconstruction accuracy were consistent with the phenomena shown in Fig. 5. The first factor was the increasing frequency when the spacing between measurement points was kept fixed. As the frequency increased, the acoustic field contained more high-wavenumber components. The highest wavenumber component, which could be captured by the array, was limited by the spacing between measurement points. As a result, the reconstruction accuracy tends to decline with the increasing frequency.

The second factor was the sound power ratio of the direct radiation relative to the boundary reflection at the measurement points, which is calculated and shown in Fig. 5(b). As the shape of the array was made conformal to the source surface in this simulation case, the accuracy in describing the directly radiated field was higher than that of the boundary-reflected field, using the half-space spherical wave function expansion with the acquired data. Hence, a higher sound power ratio generally lead to a better reconstruction result.

For a fixed vertical distance, the increasing frequency and the improved sound power ratio, as shown in Fig. 5(b), exerted opposite influences on the reconstruction accuracy. When the vertical distance $h_s = L$, for the frequencies $f = 100$ Hz $\sim$ 1300 Hz, the second factor dominated the reconstruction accuracy. As a result, the reconstruction error ε shows a decline with the increase of frequency f. When the frequency f exceeds 1300 Hz, the reconstruction accuracy is dominantly affected by the first factor, resulting in the growth of error ε.

As the vertical distance h_s increased, the plate moved away from the boundary, so that the interference from the boundary reflection gradually weakened. The sound power ratio η is improved greatly . Consequently, the reconstruction errors ε calculated at $h_s = 1.2L$, for different frequencies f, were smaller than those calculated at $h_s = L$. Similarly, the errors ε calculated at $h_s = 1.4L$ were smaller than those of the former two cases, especially in the low-frequency range. In addition, since the interference from the boundary reflection weakened, the change of η with the increasing f has less influence on ε. Hence, the curves obtained when $h_s = 1.2L$ and $1.4L$ didn't show as obvious a trend of decline as that obtained when $h_s = L$.
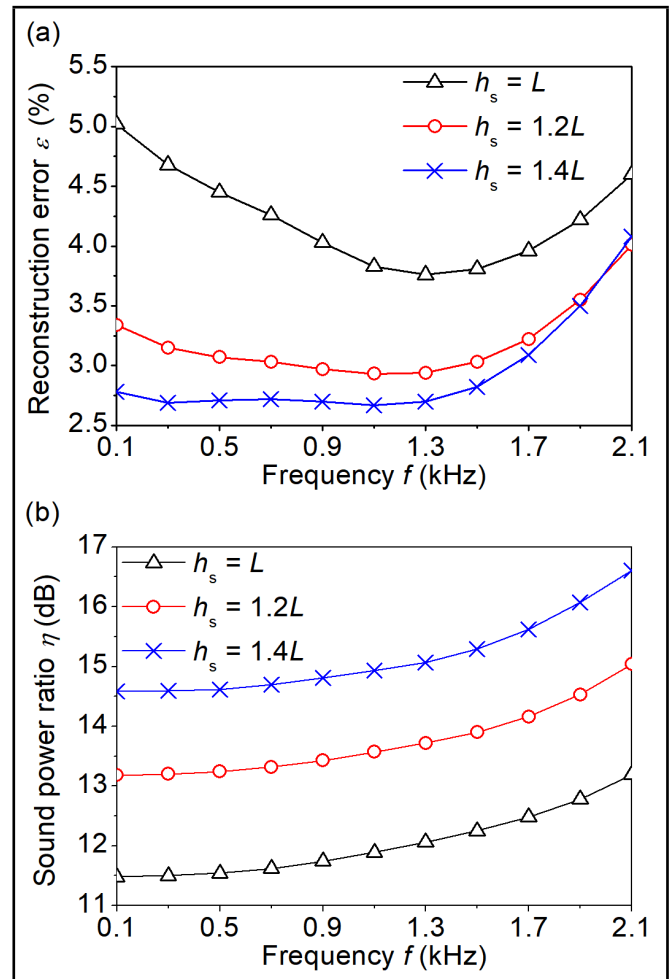
Figure 5. (a) Reconstruction errors ε and (b) sound power ratios η versus frequency f, calculated at different vertical distances h_s.

3.3. Effect of the Orientation of the Source Surface

In the simulation examples shown above, the reconstruction of the acoustic field radiated directly from a vibrating plate with the vibrating surface placed normal to the boundary was implemented. In practical applications, the angle between the plate surface and the boundary can be arbitrary. Hence, it was necessary to investigate how the reconstruction accuracy changes with the orientation of the plate surface.

A two-dimensional schematic of acoustic pressure measurements for a baffled plate with an arbitrary orientation of the vibrating surface is shown in Fig. 6. The plate and the hydrophone array were depicted by two solid lines, respectively. The angle between the plate surface and the boundary was α. Various parameters involved in the numerical simulations were chosen as follows. The length of one side of the square plate was $L = 0.4$ m, with an amplitude of surface velocity $V_0 = 1.0 \times 10^{-3}$ m/s. The plate surface was normal to the x-z plane. The distance between the geometrical center of the plate surface and the boundary was $h_s = 0.4$ m. The hologram surface was parallel to the plate surface with a standoff distance $d_s = 0.05$ m. The line defined by the geometrical centers of the two surfaces was normal to the surfaces. The aperture of the array was 0.52 m $\times$ 0.52 m, with 81 measurement points regularly distributed. The spacing between the points was 0.065 m. The reconstruction process was repeated when $\alpha = 0°$, 22.5°,
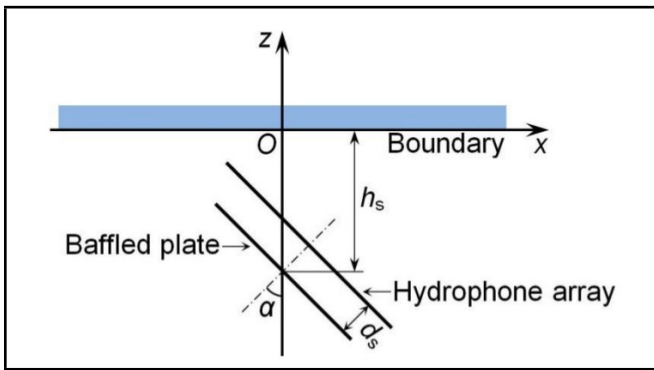
Figure 6. Two-dimensional schematic of acoustic pressure measurement for a baffled plate with an arbitrary orientation of the vibrating surface.

$45°$, $67.5°$ and $90°$. When $\alpha = 90°$, the plate was vertical. The frequencies of interest were $f = 100$ Hz ~ 2100 Hz.

Figure 7 summarizes the reconstruction errors ε and sound power ratios η versus frequency f, calculated at different orientations α of the source surface. Figure 7(a) indicates that for the frequencies $f = 100$ Hz ~ 1300 Hz, the five curves of reconstruction error ε do not show any obvious variations as the frequency changes. However, when the frequency f exceeds 1300 Hz, the five curves show completely different variation trends. For the orientations $\alpha = 0°$, $22.5°$ and $45°$, the reconstruction error ε grows drastically with the increase of frequency f. For $\alpha = 67.5°$, the growth of ε is much slower than for $\alpha = 0°$, $22.5°$ and $45°$. And for $\alpha = 90°$, ε remains around a low value like that obtained for the frequencies $f = 100$ Hz ~ 1300 Hz . The reasons behind these phenomena are described below.

In Section 3.2, it is revealed that the reconstruction accuracy is affected by two dominant factors, the frequency and the sound power ratio. For the frequencies $f = 100$ Hz ~ 1300 Hz, since the frequency f is low, various wavenumber components of the acoustic field can be fully captured by the array. Moreover, the sound power ratios η calculated at different orientations α show a small rate of variation with the increasing frequency f, as shown in Fig. 7(b). Hence, the method yields high and stable reconstruction accuracy, for the frequencies $f = 100$ Hz ~ 1300 Hz.

As the frequency f increases further, the high-wavenumber components of the acoustic field will not be well captured by the array with a fixed spacing of measurement points. In addition, the half-space acoustic pressure distributions become sensitive to the change of orientation α at high frequencies. Hence, the five curves of reconstruction error ε exhibit completely different trends for the frequencies $f = 1300$ Hz ~ 2100 Hz, as shown in Fig. 7(a). At these high frequencies, the accuracy depends heavily on the sound power ratio η, as depicted in Fig. 7(b). Specifically, the curve of reconstruction error ε shows the smallest growth rate when $\alpha = 90°$. This is because the sound power ratio η is the largest then among those calculated at the five different values of α, for each frequency f, as shown in Fig. 7(b). The largest growth rate of ε occurs when $\alpha = 22.5°$, because the corresponding sound power ratio η is very small.

The exception is the case where the orientation $\alpha = 0°$. It is found that when the frequency $f = 2100$ Hz, the sound power ratio η is the smallest among the five cases. However, the resultant reconstruction error ε is smaller than those ob-
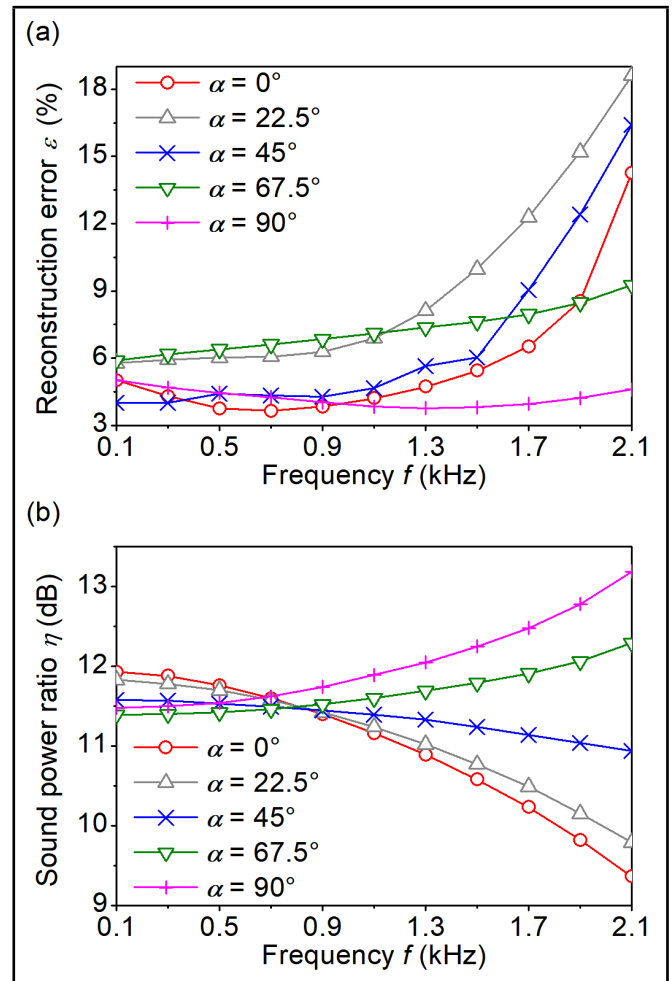
Figure 7. (a) Reconstruction errors ε and (b) sound power ratios η versus frequency f, calculated at different orientations α.

tained when $\alpha = 22.5°$ and $45°$. This is because when $\alpha = 0°$, both the hologram surface and the source surface are parallel to the boundary. Under this condition, the hologram surface is conformal to the source surface as well as the image source surface. The field radiated directly from the source and the field reflected from the boundary can simultaneously be described with acceptable accuracy using the half-space spherical wave function expansion with the acquired data. Thus, the effect of the lowest sound power ratio is offset by the optimum configuration of the hologram surface.

4. CONCLUSIONS

A method based on half-space spherical wave function expansion is proposed to reconstruct the acoustic field radiated directly from a vibrating structure located near a pressure-release boundary. The half-space spherical wave basis functions satisfying the pressure-release boundary condition are formulated. Then, the half-space acoustic field, contributed from both the source radiation and the boundary reflection, are expressed using superposition of the half-space spherical wave functions. The coefficients associated with the expansion functions are determined by solving an overdetermined system of linear equations, obtained by matching this expansion to the half-space acoustic pressures measured on a hologram surface. The acoustic field radiated directly from the source can finally be reconstructed using the free-space spherical wave functions

with the obtained expansion coefficients.

Acoustic fields generated in a water medium by a vibrating plate, located near the pressure-release boundary and in free space, are numerically simulated to validate the proposed method. The results show that the half-space acoustic pressure distribution is completely different from the benchmark distribution, implying that the measured acoustic pressures are strongly polluted due to the boundary reflection. After applying the proposed method, the reconstructed acoustic pressure distribution radiated directly from the source agrees well with the benchmark distribution. The directly radiated acoustic field at the measurement points is successfully reconstructed with high accuracy.

The effects of the vertical distance between the source and the boundary, and the orientation of the source surface, on the accuracy in reconstruction implemented at different frequencies are investigated. From the reconstruction error analyses, two dominant factors affecting the reconstruction accuracy are revealed. They are the acoustic frequency and the sound power ratio of the direct radiation relative to the boundary reflection at the measurement points. The effect of the acoustic frequency is that the reconstruction accuracy will be limited once the frequency exceeds a certain value. The effect of the sound power ratio is that the larger the ratio, the higher the accuracy tends to be. The change of vertical distance or the source orientation will lead to a varied sound power ratio. Parameters corresponding to a larger sound power ratio tend to result in higher reconstruction accuracy.

5. ACKNOWLEDGEMENTS

REFERENCES

[1] Williams, E. G. *Fourier Acoustics: Sound Radiation and Nearfield Acoustical Holography*, Academic Press, London, (1999). https://doi.org/10.1121/1.1289662

[2] Wu, S. F. Methods for reconstructing acoustic quantities based on acoustic pressure measurements, *Journal of the Acoustical Society of America*, **124**(5), 2680-2697, (2008). https://doi.org/10.1121/1.2977731

[3] Zhang, M., Hu, D. Y., Yang, Y. C., Shi, W. and Liao, A. H. An improvement of the generalized discrete Fourier series based patch near-field acoustical holography, *Applied Acoustics*, **173**, 107711, (2021). https://doi.org/10.1016/j.apacoust.2020.107711

[4] Shi, T. Y., Liu, Y. F. and Bolton, J. S. Spatially sparse sound source localization in an under-determined system by using a hybrid compressive sensing method, *Journal of the Acoustical Society of America*, **146**(2), 1219-1229, (2019). https://doi.org/10.1121/1.5122312

[5] Duffy, D. G. *Green's Functions with Applications*, CRC, New York, (2015). https://doi.org/10.1201/b18159

[6] Pierce, D. *Acoustics: An Introduction to Its Physical Principles and Applications*, Acoustical Society of America, New York, (1989). https://doi.org/10.1121/1.399390

[7] Bi, C. X., Jing, W. Q., Zhang, Y. B. and Lin, W. L. Reconstruction of the sound field above a reflecting plane using the equivalent source method, *Journal of Sound and Vibration*, **386**, 149-162, (2017). https://doi.org/10.1016/j.jsv.2016.09.029

[8] Xiang, Z. and Wu, S. F. Reconstruction of vibroacoustic fields in half-space by using hybrid near-field acoustical holography, *Journal of the Acoustical Society of America*, **117**(2), 555-565, (2005). https://doi.org/10.1121/1.1847994

[9] Zea, E. and Arteaga, I. L. Sound field separation for planar sources facing a parallel reflector, *Applied Acoustics*, **149**, 181-191, (2019). https://doi.org/10.1016/j.apacoust.2019.01.030

[10] Pan, S. W., Jiang, W. K., Zhang, H. B. and Xiang, S. Modeling transient sound propagation over an absorbing plane by a half-space interpolated time-domain equivalent source method, *Journal of the Acoustical Society of America*, **136**(4), 1744-1755, (2014). https://doi.org/10.1121/1.4895705

[11] Wu, S. F. *The Helmholtz Equation Least-Squares Method—for Reconstructing and Predicting Acoustic Radiation*, Springer, New York, (2015). https://doi.org/10.1007/978-1-4939-1640-5

[12] Zhou, D., Lu, H., McFarland, D. M. and Xiao, Y. Reconstruction of acoustic radiation of a vibrating structure located in a half-space bounded by a passive surface with finite acoustic impedance, *Journal of Theoretical and Computational Acoustics*, **28**(4), 2050019, (2020). https://doi.org/10.1142/S259172852050019X

[13] Zhou, D., Xiao, Y. and Lu, H. Reconstruction of the direct radiation from a source using the expansion in half-space spherical wave functions, *Acta Acustica*, **46**(3), 321-334, (2021) (in Chinese). https://doi.org/10.15949/j.cnki.0371-0025.2021.03.001

[14] Blackstock, D. T. *Fundamentals of Physical Acoustics*, Wiley, New York, (2000). https://doi.org/10.1121/1.1354982

[15] Marburg, S., Nolte, B., Bernhard, R. and Wang, S. *Computational Acoustics of Noise Propagation in Fluids: Finite and Boundary Element Methods*, Springer-Verlag, Berlin, (2008). https://doi.org/10.1007/978-3-540-77448-8

[16] Lu, H. and Wu, S. F. Reconstruction of vibroacoustic responses of a highly nonspherical structure using Helmholtz equation least-squares method, *Journal of the Acoustical Society of America*, **125**(3), 1538-1548 (2009). https://doi.org/10.1121/1.3068449